A *CHANDRA* OBSERVATION OF THE ULTRALUMINOUS INFRARED GALAXY IRAS 19254−7245 (THE SUPERANTENNAE): X-RAY EMISSION FROM THE COMPTON-THICK ACTIVE GALACTIC NUCLEUS AND THE DIFFUSE STARBURST

JIANJUN JIA[1], ANDREW PTAK[2], TIMOTHY M. HECKMAN[1], VALENTINA BRAITO[3], AND JAMES REEVES[4]

[1] Department of Physics and Astronomy, Johns Hopkins University, Baltimore, MD 21218, USA
[2] Goddard Space Flight Center, Greenbelt, MD 20771, USA
[3] INAF-Osservatorio Astronomico di Brera, via Brera 28, I-20121 Milano, Italy
[4] Astrophysics Group, School of Physical and Geographical Sciences, Keele University, Keele, Staffordshire ST5 5BG, UK

ABSTRACT

We present a *Chandra* observation of IRAS 19254−7245, a nearby ultraluminous infrared galaxy also known as *the Superantennae*. The high spatial resolution of *Chandra* allows us to disentangle for the first time the diffuse starburst (SB) emission from the embedded Compton-thick active galactic nucleus (AGN) in the southern nucleus. No AGN activity is detected in the northern nucleus. The 2–10 keV spectrum of the AGN emission is fitted by a flat power law ($\Gamma = 1.3$) and an He-like Fe Kα line with equivalent width $\sim$1.5 keV, consistent with previous observations. The Fe Kα line profile could be resolved as a blend of a neutral 6.4 keV line and an ionized 6.7 keV (He-like) or 6.9 keV (H-like) line. Variability of the neutral line is detected compared with the previous *XMM-Newton* and *Suzaku* observations, demonstrating the compact size of the iron line emission. The spectrum of the galaxy-scale extended emission excluding the AGN and other bright point sources is fitted with a thermal component with a best-fit kT of $\sim$0.8 keV. The 2–10 keV luminosity of the extended emission is about one order of magnitude lower than that of the AGN. The basic physical and structural properties of the extended emission are fully consistent with a galactic wind being driven by the SB. A candidate ultraluminous X-ray source is detected $8''$ south of the southern nucleus. The 0.3–10 keV luminosity of this off-nuclear point source is $\sim$6 $\times$ 10^{40} erg s^{-1} if the emission is isotropic and the source is associated with the Superantennae.

Key words: galaxies: active – galaxies: individual (IRAS 19254-7245 (the Superantennae)) – galaxies: starburst – X-rays: galaxies

Online-only material: color figures

1. INTRODUCTION

Ultraluminous infrared galaxies (ULIRGs) emit most of their total energy output in the far-infrared (FIR) domain, with an FIR luminosity greater than $10^{12}\,L_\odot$ (Sanders & Mirabel 1996). Many ULIRGs are a composite of an active galactic nucleus (AGN) and a starburst (SB), with the violent star formation activity triggered by a galaxy collision or merger (Veilleux et al. 2002, 2006). The emission from the central AGN and the dense star-forming regions is obscured by dust and gas, and the fractional contributions to the luminosity by the AGN and SB are not well constrained. Obtaining better insights into the energetics of these systems is crucial to understand the interplay between supermassive black holes (SMBHs) and the formation and evolution of galaxies, which is one of the major unsolved problems in astrophysics.

X-ray observations of ULIRGs above 3 keV, performed with *XMM-Newton* (Franceschini et al. 2003; Braito et al. 2003) and *Chandra* (Ptak et al. 2003; Teng et al. 2005) have proved to be a fundamental tool to disentangle the contribution of SB and AGN activity and to investigate the presence of hidden AGNs in these sources. Indeed some of the ULIRGs, classified as pure SBs based on optical and IR spectroscopy, show spectral properties typical of obscured AGNs only when observed in X-rays (i.e., NGC 6240: Iwasawa & Comastri 1998; Arp 299: Della Ceca et al. 2002). Previous X-ray surveys of ULIRGs have also shown that thermal emission from a hot plasma with a rather constant temperature $kT \sim 0.7$ keV is always present (Grimes et al. 2005). This emission dominates the X-ray spectra below 1 keV and it is likely associated with a nuclear or circumnuclear SB.

In particular, *Chandra* observations of luminous and ULIRGs have proved to be essential to investigate the spatial structure and physical properties of this soft diffuse X-ray emission. Thanks to its high spatial resolution, *Chandra* observations have shown that in ULIRGs, like in local SBs, this soft diffuse emission extends far beyond the SB region itself. This emission is primary evidence of the presence of galactic superwinds (Chevalier & Clegg 1985; Heckman et al. 1993; Strickland & Stevens 2000), which are believed to play a major role in the evolution of galaxies and metal enrichment of the intergalactic medium. However, these studies have also shown that ULIRGs are faint X-ray sources, thus an X-ray follow-up is feasible only for the very brightest ones.

Understanding the physical processes at work in ULIRGs is important since observational evidence shows that ULIRGs are generally advanced mergers of gas-rich galaxies, which are considered to be the origin of many massive elliptical and S0 galaxies. If indeed ULIRGs are forming spheroids, an AGN/SB association is naturally supported by the evidence that all spheroidal galaxies host quasar relics in the form of SMBHs, and the quasar stage could be a phase during the evolution of these systems. Support for this view has come from high-resolution spectroscopy of ULIRG mergers (Genzel et al. 2001), whose dynamical properties have proved that they indeed are "ellipticals in formation." In this framework high-resolution simulations of galaxies mergers (Hopkins et al. 2006; Springel et al. 2005) have shown that galaxy mergers may play a fundamental role in SMBH growth and galaxy evolution. Indeed, the merger provides the inflow of gas that is likely to fuel both the SB and, at some stages, an AGN.

These simulations predict that for most of this phase the AGN is obscured, with the optically visible AGN phase occurring in the late stages when the SB and/or AGN essentially explosively drives out all the remaining interstellar material in the system. To test the predictions of the evolutionary sequence more robust star formation rate (SFR) and AGN activity estimators are needed. This reinforces the importance of understanding the contributions of SB and AGN activity in known examples in which they coexist.

Like most ULIRGs, IRAS 19254−7245, at $z = 0.062$, is a merger system of two gas-rich spiral galaxies, with the nuclei $\sim 9''$ (which corresponds to ~ 11 kpc; Berta et al. 2003) apart from each other. Among these interacting ULIRGs, IRAS 19254−7245, with $L_{FIR} = 2 \times 10^{12} L_\odot$, is a remarkable one (Mirabel et al. 1991; Genzel et al. 1998). It is known to host a powerful SB with SFR $\sim 80 M_\odot$ yr^{-1} (Berta et al. 2003) and a heavily obscured AGN (Mirabel et al. 1991), which resembles in many aspects the prototypical type-II (obscured) quasar NGC 6240 (Iwasawa & Comastri 1998). This source exhibits giant tidal tails extending to a distance of about 350 kpc triggered by a merger event reminiscent of the classical "*Antennae*" seen in NGC 4038/4039. The northern galaxy shows an optical spectrum typical of SB (Berta et al. 2003).

Previous X-ray observations of IRAS 19254−7245 (Pappa et al. 2000; Braito et al. 2003) strongly support the features observed in optical and IR bands. A recent *Suzaku* observation has detected the intrinsic AGN emission in the 15–30 keV band and has confirmed the *XMM-Newton* detection of Fe–Kα emission (Braito et al. 2009). These data show that both neutral and ionized Fe–Kα lines are present. In this scenario, the intrinsic 2–10 keV luminosity of IRAS 19254−7245 could be greater than 10^{44} erg s^{-1}, dominated by the buried quasar. This picture has been confirmed by high signal-to-noise L band (3–4 μm; Risaliti et al. 2003) and *Spitzer* observations (Nardini et al. 2008), which also suggested that the main energy source in the mid-IR is an obscured AGN. The *XMM-Newton* and *Suzaku* observations have also shown that the soft emission is dominated by the SB. The temperature ($kT \sim 0.85$ keV) and the luminosity of this soft component ($\sim 2 \times 10^{41}$ erg s^{-1}) are consistent with the hot gas found in SB galaxies and in the other ULIRGs observed so far. The *XMM-Newton* data show that, although the X-ray emission comes mostly from the southern nucleus containing the buried AGN, the source is slightly extended. However, the *XMM* point-spread function (PSF) was too broad to allow the structure of the soft X-ray emission to be investigated in more detail. Furthermore, since the smallest possible extraction region with *XMM-Newton* includes the whole system, it was not possible to spatially disentangle the contribution of diffuse SB and AGN emission. Again despite the intrinsic high luminosity of the AGN in IRAS 19254−7245, it is heavily obscured and thus it may not outshine the SB emission below 2 keV.

Here, we present the analysis of three exposures of IRAS 19254−7245 by *Chandra* with total exposure time of 75 ks. These are the first X-ray observations that allow us to directly disentangle the AGN and SB. We present the *Chandra* data reduction in Section 2, and we analyze and fit the spectra of the different parts of IRAS 19254−7245 in Section 3. We then discuss our results and draw conclusions in Section 4.

2. OBSERVATIONS AND DATA REDUCTION

The *Chandra X-ray Observatory* observed IRAS 19254−7245 for three separated exposures with the back-illuminated chip S3 of the Advanced CCD Imaging Spectrometer (ACIS)

Table 1
Observation Log

ObsID	Date (YYYY-MM-DD)	Exp. Time[a] (ks)
10538	2009-12-14	29.06
11797	2009-12-19	35.16
11798	2009-12-19	11.81

Note. [a] The exposure time is the good time interval after flare filtering.

instrument in a `FAINT` mode in 2009 December (see Table 1). The data were reprocessed using the contributed script `chandra_repro` of the CIAO software (ver. 4.3) and calibration database (CALDB 4.4.2) to create the new Level 2 event files (Fruscione et al. 2006). Sources were detected using the `wavdetect` tool.

In Figure 1, we show four images of IRAS 19245−7245 by merging the three observations, which are within the energy bands of (1) 0.3–2 keV, (2) 2–4 keV, (3) 4–8 keV, and (4) 6–7 keV, where 6–7 keV samples the Fe–K line region of the spectrum, and the other bands sample regions when SB versus AGN emission is expected to be in decreasing proportion. The images are smoothed (in `ds9`) with a Gaussian kernel of 3 pixels (1″.5 in radius, where 1″ corresponds to 1.2 kpc at the redshift of IRAS 19245−7245). We marked the southern (S), northern (N) nucleus and an off-nuclear point source (X1) in panel (b). In panel (a) of Figure 1, we divided the diffuse emission into two regions in shape of annuli with their origin at the southern nucleus: D1 (3″–10″, i.e., 3.5–11.8 kpc) and D2 (10″–20″, i.e., 11.8–23.6 kpc). In the following subsections, we will analyze the images and spectra of the nuclei and the diffuse emission.

Throughout the work in this paper, all *Chandra* spectra as well as the associated response (RMF) and ancillary (ARF) files were extracted by running the script `specextract`, which has slightly different input parameters for point-like source and extended emission. We adopt cosmological parameters of $H_0 = 70$ km s^{-1} Mpc^{-1}, $\Omega_M = 0.27$, and $\Omega_\Lambda = 0.73$.

3. ANALYSIS

3.1. The Entire Merging System

IRAS 19254−7245 was observed by *XMM-Newton* in 2001 March (Braito et al. 2003) and *Suzaku* in 2006 November (Braito et al. 2009). The published X-ray fluxes and spectral properties were derived from spectral analysis of the global emission (here "global" means the entire region including the two nuclei and the extended SB region). We thus first analyzed the global spectra of our *Chandra* observation, and compared them with the *XMM* and *Suzaku* observations to see whether there is any variability. The radius of the extraction region is 15″, centered on the southern nucleus, which follows the work of the *XMM* observation. The source region in the *Suzaku* paper has a radius of $\sim 2'.9$, which covers nearly the entire S3 chip. There are several visually detected point sources that are located 1′–3′ away from the southern nucleus of IRAS 19254−7245. Therefore, we did not use this source radius to extract the global spectra. The background emission was chosen from a close-by source-free circular region.

The effective exposure time after flare filtering is shown in Table 1. Photons with energy greater than 8 keV were ignored in the spectral fitting, since the effective area of the ACIS chips is very small above 8 keV. We obtained 1850 photons in total for all three exposures. The spectrum of each observation was
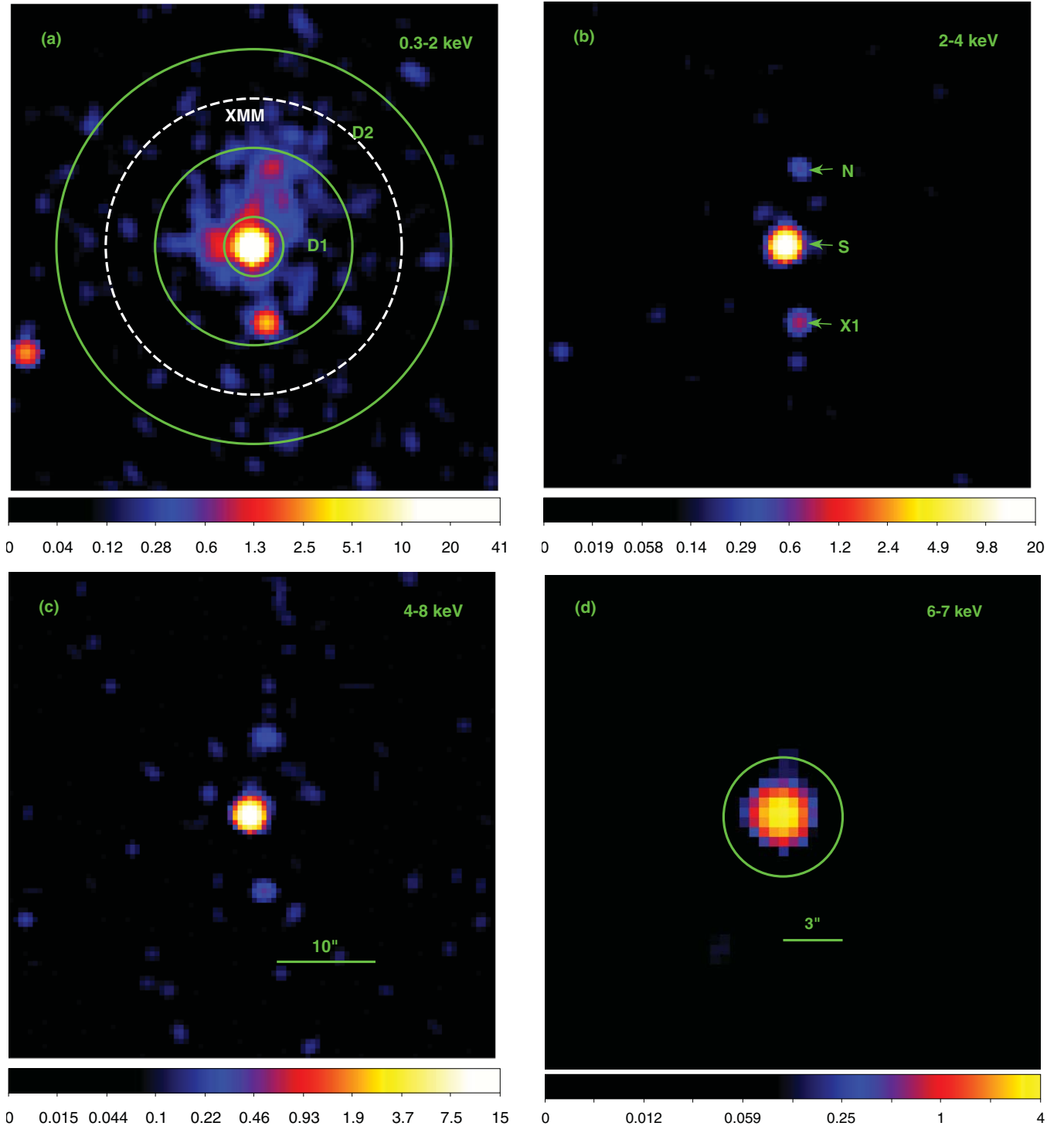
Figure 1. *Chandra* images of IRAS 19245−7245 in the energy bands of (a) 0.3–2 keV, (b) 2–4 keV, (c) 4–8 keV, and (d) 6–7 keV. North is up, and east is left. These images are merged from the three separated exposures, and smoothed using a Gaussian function with kernel radius of 3 pixels. The annuli of D1 (3″–10″) and D2 (10″–20″) are indicated by the green circles, and the dashed white circle indicates the extraction region (15″) in *XMM* observation (Braito et al. 2003). The southern (S) and northern (N) nuclei are marked in panel (b), as well as one off-nuclear point source (X1). Panels (a)–(c) are in the same scale that is indicated in panel (c), and panel (d) has a different spatial scale for illustration.

(A color version of this figure is available in the online journal.)

grouped to at least 10 counts per bin to allow the use of χ^2 statistics.

Following the work of Braito et al. (2003, 2009), we fit each spectrum using a model of thermal plus power law (PL) with an additional Fe Kα line. The weighted average Galactic H I column density is $N_{\rm H,G} = 5.95 \times 10^{20}$ cm^{-2} (Dickey & Lockman 1990; Kalberla et al. 2005), and is set to be the lower boundary of the obscuration during the fit. We fixed abundance in the thermal component to solar. The photon index of the PL continuum was determined by ignoring photons with energy greater than 6 keV, to avoid biasing the continuum model due to Fe–K emission. We then fixed the photon index at the value
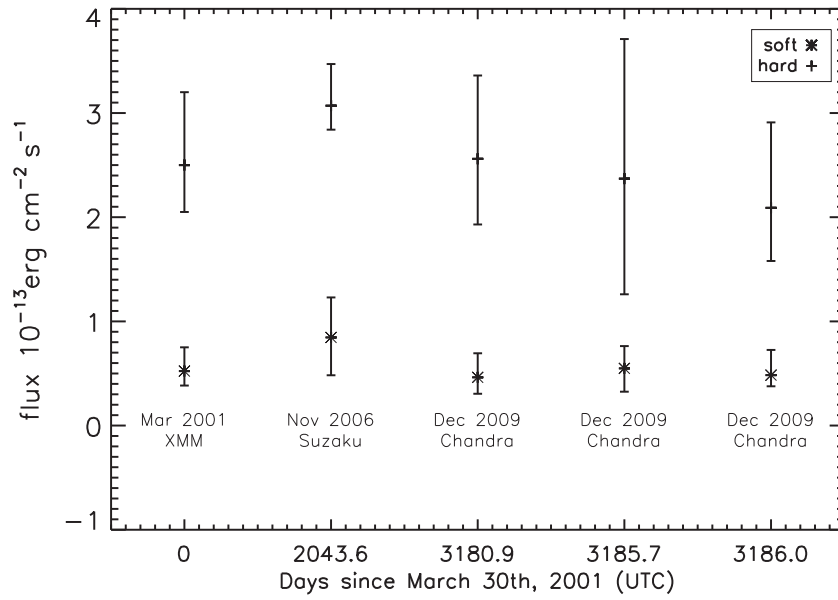
Figure 2. Soft (asterisk) and hard X-ray (plus) fluxes of each observation. The points correspond in chronological order to *XMM*, *Suzaku*, and *Chandra* observations. X-axis indicates the days since the date of *XMM* observation, and is not in linear scale.

Table 2
X-Ray Spectral Model Parameters

Region	N_H[a]	kT[b]	Γ[c]	E_{Fe}[d]	σ[e]	EW[f]	χ^2/ν or C/ν	$L_{SX,th}$[g]	$L_{SX,pl}$[h]	L_{HX}[i]	L_{Fe}[j]
Global[k]	$1.84^{+2.75}_{-1.43}$	$0.72^{+0.12}_{-0.14}$	$1.30^{+0.18}_{-0.16}$	$6.68^{+0.14}_{-0.08}$	$0.13^{+0.17}_{-0.09}$	$1.71^{+0.90}_{-0.74}$	146.0/154	$1.3^{+2.1}_{-0.7}$	$2.7^{+0.8}_{-0.7}$	$22.6^{+7.0}_{-5.5}$	$4.1^{+2.1}_{-1.8}$
Global[l]	$1.29^{+0.77}_{-0.45}$	$0.77^{+0.06}_{-0.07}$	$1.26^{+0.09}_{-0.07}$	$6.68^{+0.05}_{-0.05}$	$0.17^{+0.06}_{-0.05}$		388.9/361	$1.7^{+0.8}_{-0.4}$	$3.6^{+0.4}_{-0.2}$	$22.7^{+2.4}_{-1.3}$	
S (joint)	$3.35^{+1.57}_{-1.22}$	$0.79^{+0.39}_{-0.23}$	$1.28^{+0.25}_{-0.17}$	$6.68^{+0.12}_{-0.11}$	$0.23^{+0.50}_{-0.23}$	$1.52^{+1.01}_{-0.73}$	81.7/103	$0.7^{+0.4}_{-0.2}$	$2.1^{+0.6}_{-0.2}$	$19.4^{+5.3}_{-2.1}$	$3.3^{+1.4}_{-1.2}$
S (summed)	$5.26^{+2.87}_{-2.63}$	$0.79^{+0.29}_{-0.19}$	$1.22^{+0.19}_{-0.21}$	$6.69^{+0.22}_{-0.12}$	$0.24^{+0.29}_{-0.13}$	$1.50^{+0.44}_{-0.60}$	99.1/97	$0.9^{+1.1}_{-0.5}$	$1.7^{+0.3}_{-0.3}$	$19.8^{+3.9}_{-3.3}$	$3.3^{+1.0}_{-1.3}$
N	$2.49^{+7.04}_{-2.49}$		$1.25^{+0.93}_{-1.23}$				25.5/29		$0.10^{+0.05}_{-0.04}$	$0.48^{+0.25}_{-0.19}$	
D1	$0.69^{+0.94}_{-0.69}$	$0.78^{+0.13}_{-0.07}$	$1.73^{+0.60}_{-0.56}$				23.1/26	$0.58^{+0.69}_{-0.24}$	$0.4^{+0.26}_{-0.18}$	$0.88^{+0.59}_{-0.41}$	
D2	$N_{H,G}$	$0.90^{+0.46}_{-0.27}$	$2.70^{+0.87}_{-0.88}$				28.5/28	$0.17^{+0.11}_{-0.11}$	$0.25^{+0.15}_{-0.17}$	$0.15^{+0.09}_{-0.10}$	
D1+D2	$1.10^{+0.98}_{-1.02}$	$0.77^{+0.08}_{-0.11}$	$1.79^{+0.75}_{-0.59}$				53.8/55	$0.86^{+0.67}_{-0.30}$	$0.49^{+0.35}_{-0.22}$	$1.15^{+0.82}_{-0.52}$	

Notes. Uncertainties correspond to the 90% confidence level for one interesting parameter.
[a] Column density in units of 10^{21} cm^{-2}.
[b] Temperature of thermal plasma in keV.
[c] Photon index of hard continuum.
[d] Energy of line center in keV in rest frame.
[e] Emission line width in keV.
[f] Equivalent width of emission line in keV.
[g] Soft X-ray luminosity contributed by thermal plasma in units of 10^{41} erg s^{-1}.
[h] Soft X-ray luminosity contributed by power-law continuum in units of 10^{41} erg s^{-1}.
[i] Hard X-ray luminosity in units of 10^{41} erg s^{-1}.
[j] Iron emission line luminosity in units of 10^{41} erg s^{-1}.
[k] Using stacked spectral data from *Chandra* observation.
[l] Using *Chandra*, *XMM*, and *Suzaku* data.

we obtained and added the photons in energy band 6–8 keV to fit the iron emission line. Fixing the photon index reduces the degeneracy of model parameters in spectral fitting. However, we also fitted the spectrum with free parameters for both continuum and line components in the full band including the thermal component, and the results were very close to those above.

We plot the 0.5–2 keV and 2–10 keV fluxes of the *Chandra* and the other two observations by *XMM* and *Suzaku* in Figure 2. The observed X-ray luminosities reported in *XMM* observation (Braito et al. 2003) were about a factor of two higher because of the cosmological parameters used in their paper, so we re-derived the luminosities by using the latest parameter values above.

There were no significant variations in the spectral shape of the individual *Chandra* observations, and spectral parameters like the photon index have values consistent with the errors, but with larger uncertainties in ObsID 11798, which had the shortest exposure time. Therefore, we combined the spectra in order to get tighter constraints. The spectra were summed using addspec in HEASoft FTOOLS. Again, the combined spectra were grouped to at least 10 counts per bin, and χ^2 statistics were used in the fitting. The best-fitting parameters are shown in Table 2, as well as the observed soft and hard X-ray luminosities contributed by each component, where errors are determined at the 90% confidence level for one parameter of interest.
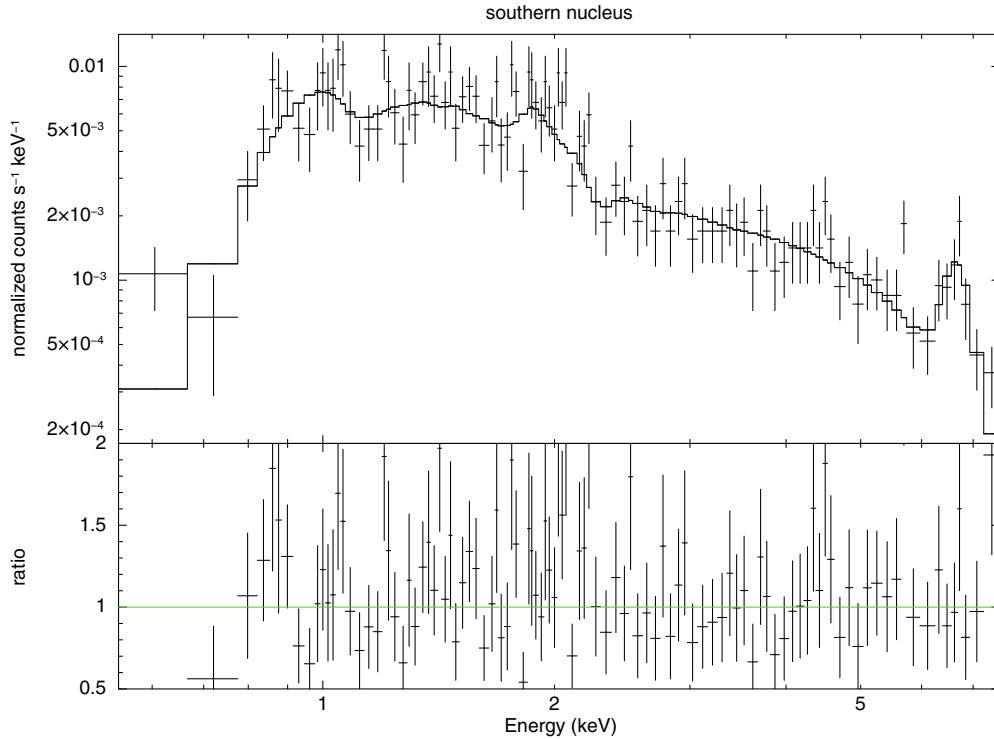
Figure 3. *Chandra* spectrum of the southern nucleus. The spectral model consists of a thermal, a power-law, and an emission line component. Photon energy is de-redshifted to the rest frame. Top: data and the model; bottom: ratio of data to model.
(A color version of this figure is available in the online journal.)

In order to derive tighter spectral constraints, we included the *XMM* and *Suzaku* data by fitting the spectra simultaneously, resulting in a time-averaged fit. The parameters of the thermal and PL components were tied together in different spectral groups except for the relative normalization via a constant multiplicative factor. The temperature and PL index parameters from this spectral fit of all three observations were close to the results using *Chandra* observation only but with smaller uncertainties, as shown in Table 2. The luminosities were calculated as the mean of the three observations. The plasma abundance was initially fixed at solar, and we then allowed it to vary as a free parameter in this fit. The best-fit abundance was $Z = 0.34\ Z_\odot$ but was poorly constrained. We thus fix this parameter to be at solar in this and the following spectral analysis. We first tied the normalization of the iron line component in all three observations, and the line energy was found to be at 6.68 ± 0.05 keV, consistent with the above spectral fit using *Chandra* observations only. However, the line equivalent width (EW) was only $\sim 0.78^{+0.18}_{-0.25}$ keV from the joint fit to *XMM/Suzaku/Chandra*, compared with EW $= 1.71^{+0.90}_{-0.74}$ keV obtained above from *Chandra* data alone, which suggests there is variability of the iron line emission. Thus, we allowed the normalization of the iron line component to be free between the three groups. As the EW and luminosity of iron line differ between three observations, we left them as blank in Table 2, and we will discuss the variability in the following sections.

3.2. Southern Nucleus

The southern nucleus is known to host a Compton-thick AGN by previous X-ray observations (Pappa et al. 2000; Braito et al. 2003, 2009). Those X-ray satellites have low spatial resolution, and the detected X-ray emission from the AGN was contaminated by the host galaxy. We are now able to disentangle

the AGN from its nuclear SB region in our *Chandra* observation. We extracted the spectra of the AGN in the southern nucleus from a circular cell with radius $2''.5$, where we got 1274 photons in total for three exposures. The nucleus is a point-like source, so an energy-dependent point-source aperture correction was applied to the source ARF file. A local background spectrum was extracted from an annulus centered on the nucleus with an inner radius of $3''$ and an outer radius of $4''$.

We performed a joint spectral fit to the spectra from all three exposures, initially with an absorbed PL plus a Gaussian model. Then, an additional thermal component (APEC) was added to the fit. The abundance was again fixed at the solar value, and we found a best-fit temperature of the plasma $kT = 0.79^{+0.39}_{-0.23}$ keV. χ^2 decreased from 90.0 for 105 degrees of freedom (dof; without the thermal component) to 81.7 for 103 dof. Compared to the PL plus Gaussian model, this model was preferred at 99.3% confidence level according to the *F*-test.

We also fit the summed spectrum and the spectral parameters are close to the joint fit above. We list the best-fitting parameters of both the joint fit and the summed-spectrum fit in Table 2. The summed spectrum is shown in Figure 3. The strong iron emission line at $6.69^{+0.22}_{-0.12}$ keV with an EW of $1.50^{+0.44}_{-0.60}$ keV is consistent with the previous X-ray observations. Since the flat continuum ($\Gamma \sim 1.2$) of the hard X-ray spectrum below 10 keV may be due to reflection by Compton-thick material (Braito et al. 2003, 2009), we added a reflection component PEXRAV (Magdziarz & Zdziarski 1995) with its intrinsic PL index tied to the scattered PL component to the fit. However, this did not result in a statistically significant change to the PL slope or iron line EW.

An interesting question is whether the soft flux in this spectrum is due to circumnuclear SB emission or is more directly associated with the AGN. To test how this emission scales with extraction region size, we also extracted the spectrum of
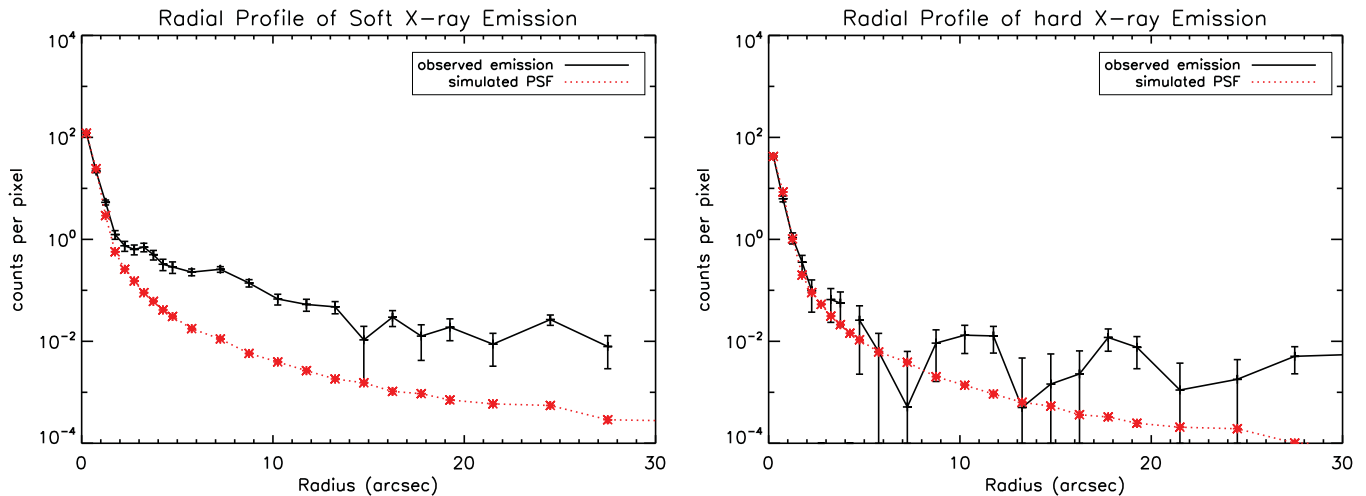
Figure 4. Radial count distributions of the observed extended structure from the centroid of the southern nucleus (in black) and the simulated PSF (in red) in both soft (left) and hard (right) X-ray bands.

(A color version of this figure is available in the online journal.)

southern nucleus in a smaller region with a radius of $1\rlap{.}''5$, which reduced the photon counts to 1183. However, the background was extracted from the larger source region (with radius = $2\rlap{.}''5$, the same region as the source extraction region above), scaled to the area of the $1\rlap{.}''5$ circle. The rationale is that any component that is extended over the $2\rlap{.}''5$ region with a constant surface brightness would subtract out completely, while nuclear point-like emission would be reduced only by the ratio of the areas of the two regions, i.e., $1.5^2/2.5^2 \sim 1/3$. The temperature of the thermal component is $kT = 0.78^{+0.40}_{-0.48}$, nearly the same as the value above but with larger uncertainty. The PL normalization is two-thirds of that in the spectral fit of the larger extraction region case, and so is the iron line normalization, consistent with both of these components being point-like. The ratio for the APEC normalization holds the same scaling relationship as that of the PL normalization in the two cases. This indicates that either there is also point-like emission, i.e., dominated by a thermal source, in the innermost part of the nucleus or the AGN emission is mixed with the ambient star formation and we cannot resolve it with *Chandra*. If the latter is true, we would expect consistency with the diffuse emission from the extended SB region, which we will analyze in Section 3.4 below.

3.3. Northern Nucleus

Although the northern nucleus is relatively weak in X-ray emission compared with the southern one and is believed not to harbor an AGN, it is still interesting to investigate its X-ray properties. We positioned the northern nucleus by visual examination and extracted the spectra within a circle of radii of $1\rlap{.}''5$ for ObsIDs 10538 and 11797. It could not be visually detected in the observation of ObsID 11798, and the spectrum was extracted from the region used in ObsID 10538, which has the brightest northern nucleus in three exposures. Thirty photons in total are collected in 0.3–8 keV range. We summed the spectra and fitted the combined spectrum with an absorbed PL model using the Cash statistic (Cash 1979). Although the Cash statistics is designed for unbinned data, we grouped the spectra to at least 1 count per bin, which could improve the performance of the fit (Teng et al. 2005). The photon index is found to be $\Gamma = 1.25^{+1.23}_{-0.93}$. The observed 2–10 keV luminosity

derived from this model is $L_{2-10\,\mathrm{keV}} = 4.8^{+2.5}_{-1.9} \times 10^{40}$ erg s^{-1}. The spectral parameters are listed in Table 2.

3.4. Diffuse Emission

3.4.1. Imaging

Thanks to the high spatial resolution of *Chandra* the diffuse emission from the star formation regions could be imaged (see Figure 1). In order to study the extended structure, we investigated the brightness distribution of IRAS 19254−7245. We first simulated an observation of a point source with the same spectral properties as the merged event using the *Chandra* Ray Tracer (Carter et al. 2003) to trace the rays through the *Chandra* X-ray optics, and created an image of the PSF using MARX (version 4.5). The comparison between the observed radial profile of the extended structure and the simulated PSF in both soft and hard X-ray bands is shown in Figure 4, where the X-ray centroid of the southern nucleus was used as the origin. In the left panel of Figure 4, we see that the observed distribution of the soft X-ray emission is rather close to the simulated one within the radius of $\sim 2''$, and for radii between $3''$ and $20''$, there is a significant excess of the observed counts with respect to the simulated PSF. In the hard X-ray band shown in the right panel of Figure 4, the radial profile of the extended emission is consistent with the simulated PSF.

3.4.2. Spectral Analysis

In order to extract the spectrum of the circumnuclear SB, the emission from the AGN was excised within a circle of $3''$ radius, and other point sources detected by `wavdetect` were also excluded (also with $3''$ regions). We extracted the spectra of the star-forming region in two annuli centered on the southern nucleus: one has the inner radius of $3''$ and outer radius of $10''$ (D1); the other one has inner radius of $10''$ and outer radius of $20''$ (D2), as described in Section 2. The background spectra were extracted in a concentric annulus with inner radius of $40''$ and outer radius of $50''$. The spectra of three exposures were then added to improve the signal-to-noise ratio.

Soft emission. The extended star-forming region is dominated by soft emission, as shown by the comparison between the soft and hard X-ray images in Figure 1. The photon counts were
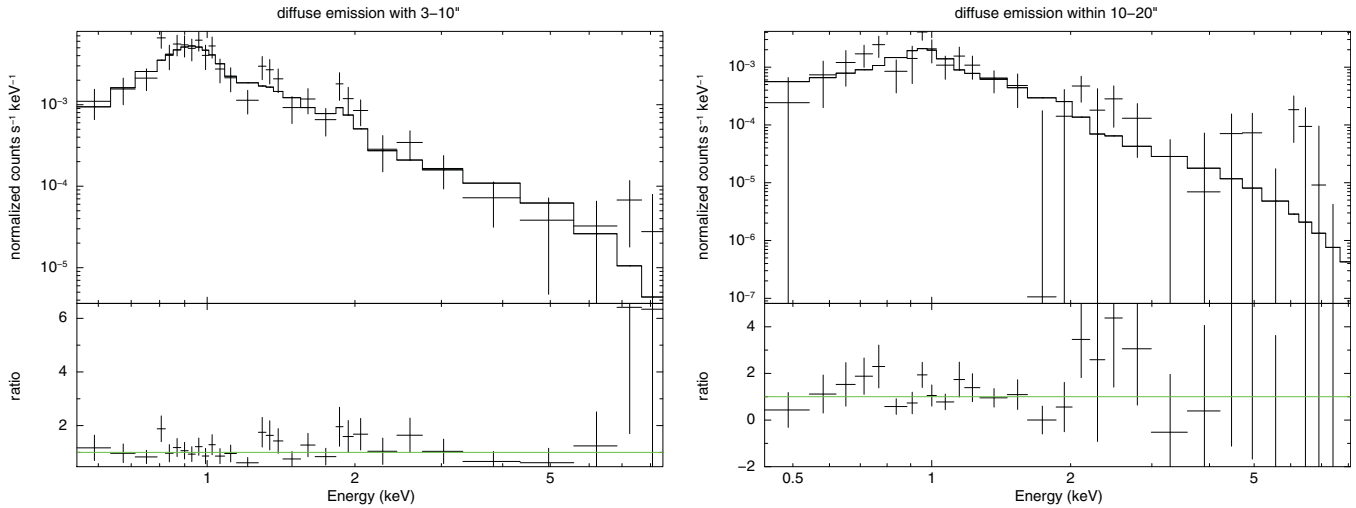
Figure 5. Spectral fits of the diffuse emission in annuli of 3″–10″ (left) and 10″–20″ (right), where the southern nucleus is at the center.
(A color version of this figure is available in the online journal.)

Table 3
Spectral Fits Parameters of the Thermal Component in Diffuse Emission

Region	$N_{H,1}$ $(10^{21}\ cm^{-2})$	kT_1 (keV)	K_1[a]	$N_{H,2}$ $(10^{21}\ cm^{-2})$	kT_2 (keV)	K_2[a]	χ^2/ν
			Single temperature				
D1	$N_{H,G}$	$0.77^{+0.08}_{-0.09}$	$4.0^{+1.2}_{-0.8} \times 10^{-6}$				19.15/22
D2	$N_{H,G}$	$0.91^{+0.48}_{-0.60}$	$1.2^{+1.0}_{-1.0} \times 10^{-6}$				18.9/17
			Double temperatures				
D1	$21.9^{+29.7}_{-10.2}$	$0.34^{+0.23}_{-0.06}$	$3.5^{+190}_{-3.0} \times 10^{-4}$	$N_{H,G}$	$0.76^{+0.07}_{-0.09}$	$4.8^{+0.8}_{-1.0} \times 10^{-6}$	15.2/19
D2	$0.75^{+7.25}$	$0.27^{+0.18}_{-0.12}$	$2.4^{+960}_{-1.8} \times 10^{-6}$	$3.54^{+4.36}_{-3.54}$	$0.95^{+0.45}_{-0.24}$	$4.0^{+7.1}_{-3.0} \times 10^{-6}$	18.1/13

Note. [a] Plasma model normalization in units of $10^{-14}/\{4\pi[D_A(1+z)]^2\}\int n_e n_H dV$, where D_A is the angular distance, and n_e and n_H are the electron and hydrogen number densities, respectively.

about 350 each in D1 and D2, and we grouped them to 10 counts per bin to use χ^2 statistic. We fitted the spectra using a thermal plus PL model, and the abundance was initially frozen to solar. The resulting temperature was $kT = 0.77^{+0.08}_{-0.09}$ keV for D1 and $kT = 0.91^{+0.48}_{-0.60}$ keV for D2 (see Table 3). The plasma temperatures are consistent with the spectral fits of *XMM* and *Suzaku* data, and are within the typical range of SB galaxies (e.g., Ptak et al. 1999; Grimes et al. 2005). The temperature of the diffuse emission in D1 is also close to the value for the AGN spectra, indicating that the emission from the southern nucleus is probably also exhibiting thermal emission from the circumnuclear star-forming regions. We then investigated the possibility of introducing another thermal component associated with an absorber in the spectral fitting since such a feature is found in other ULIRGs (Dahlem et al. 1998; Iwasawa & Comastri 1998; Gallagher et al. 2002). This second plasma component is colder, with a temperature of $kT = 0.34^{+0.23}_{-0.06}$ keV for D1 and $kT = 0.27^{+0.18}_{-0.12}$ keV for D2. The best-fitting parameters are listed in Table 3. The two-temperature model does not improve the spectral fit much ($\Delta\chi^2 = 4$ for 4 fewer degrees dof, Table 3), and the normalization of the cooler component has a very large uncertainty, so we thus adopt the results of the single temperature model in this paper.

Hard emission. In our spectral fits, the hard continuum was dominated by a PL component. For the inner region D1, the photon index is $1.73^{+0.60}_{-0.56}$, a typical value for AGN. For the outer

region D2, we initially got a much steeper index of $2.70^{+0.87}_{-0.88}$. However, the larger errors due to low signal to noise makes it consistent with the value in the spectral fit of D1. Using the simulated PSF of the central AGN, we counted about 10 photons in D1 region, while the number of total 2–10 keV photons in D1 is about 50. Roughly assuming the PSF wing photons have the same count-to-flux coefficient as the diffused emission, we estimated that the southern nucleus PSF wing contribution to hard X-ray luminosity is ∼20% in D1 and negligible in D2 (the PSF wing goes below background level in D2). The soft and hard X-ray luminosities are also listed in Table 2, and the spectral plots of both regions are shown in Figure 5. As we see in Table 2, the thermal emission and PL emission account for similar amounts of the soft X-ray emission. The hard X-ray luminosity is 20 times smaller than that of the southern nucleus. The best-fit column density along the line of sight is negligible in D2 so we set it to be equal to the Galactic column density, and it is slightly larger in D1. Because the hard X-ray emission in the D2 is much weaker than in D1 and has poorer quality, we extracted the spectra from the combined regions of D1 and D2 and re-fitted the hard spectrum. The PL index was then found to be close to that in D1.

The spectrum of the diffuse emission shows an excess in the 6–7 keV band. Could it be due to ionized iron emission contributed by very hot gas driven by the SB (Heckman et al. 1990; Strickland & Heckman 2007)? We show in panel (d) in
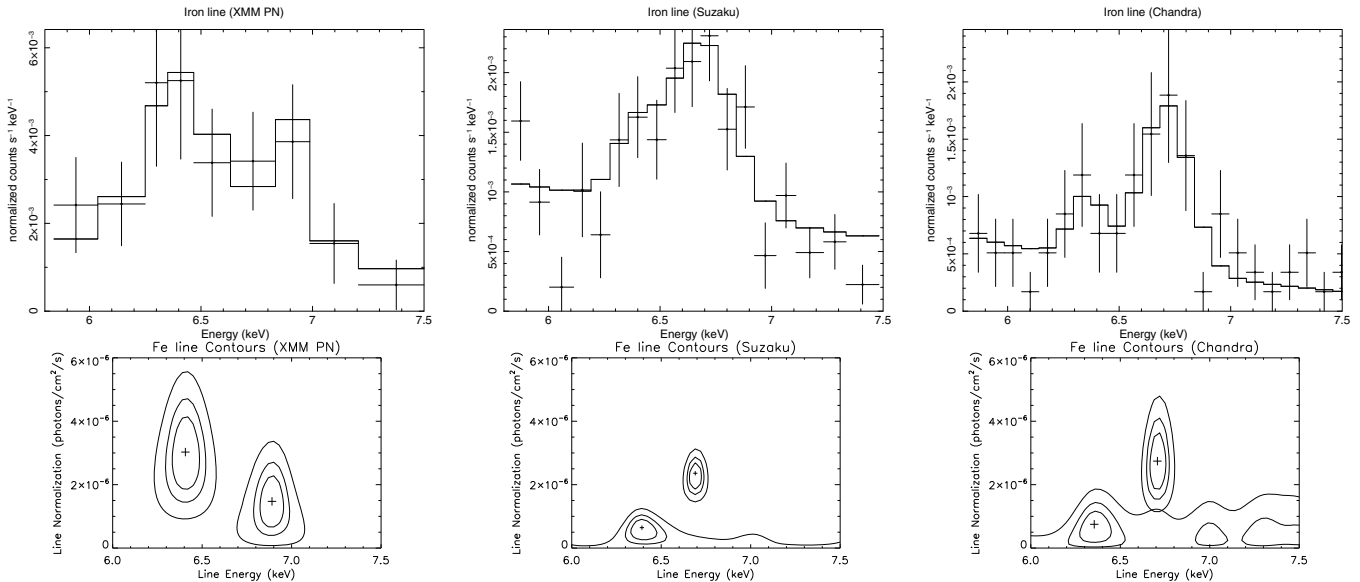
Figure 6. Upper: iron emission line profile fitted by double Gaussian lines centered for the *XMM*, *Suzaku*, and *Chandra* observations. The energy is de-redshifted to the rest frame; Lower: confidence contour plots for the double Gaussian lines profile. Contours correspond to the 68%, 90%, and 99% confidence levels, respectively.

Figure 1 the image within the energy range of 6.0–7.0 keV, which covers the neutral and ionized iron emission line energies in observer's frame. This image shows that the region of iron line emission overlaps the southern nucleus and is not extended. However, due to the low signal-to-noise ratio and limited photons in hard X-ray band, we cannot rule out the possibility that the hard continuum emission is due to another much hotter plasma. If we fit the hard X-ray spectrum with a thermal component, the temperature is $kT \sim 6$ keV with very large uncertainty, and the reduced χ^2 is nearly the same as that in the case of PL.

3.5. Iron Line Emission

The iron emission line in the southern nucleus has a relatively broad profile ($\sigma \sim 0.3$ keV), and Braito et al. (2009) showed the possibility that it is a blend of multiple lines. It is therefore interesting to further investigate this feature. In order not to wash out the possible fine structure of the iron line profile, we fitted the unbinned time-averaged *Chandra* spectra using the Cash statistic.

We used a PL continuum with the photon index fixed at $\Gamma = 1.22$ and two Gaussian lines to fit the *Chandra* spectrum within energy between 3 keV and 8 keV. The centroid energy of two lines are found to be $6.43^{+0.37}_{-0.36}$ and $6.71^{+0.07}_{-0.03}$ keV, and the EWs are $0.17^{+0.17}_{-0.17}$ keV and $0.66^{+0.41}_{-0.26}$ keV, respectively, i.e., the neutral iron line is weaker than the ionized iron line. However, this is not the same as when we re-analyzed the *XMM* data. We fitted the unbinned PN data of the *XMM* observation in the same way as above. The energy of the ionized iron line is $6.89^{+0.07}_{-0.08}$ keV, which is nearly hydrogen-like. The EW is $1.16^{+0.94}_{-0.50}$ keV for the neutral line, and $0.44^{+0.32}_{-0.33}$ keV for the ionized line. The double line fit of *Suzaku* data gives similar results as *Chandra* for the line energy and EW as the *Chandra* observation. We then plotted the confidence contours between the line energy and normalization for both lines at the 1σ, 2σ, and 3σ levels. The line profile and contours are shown in Figure 6, where the energy is in the rest frame. We see that the significance of the 6.4 keV line in *Suzaku* and *Chandra* observations is only 2σ, but the lines in the *XMM* observation could be separately detected at >99% confidence.

We then ran Markov Chain Monte Carlo (MCMC) simulations to test the statistical significance of the lines. Each chain entailed 10^5 iterations, and we ran five chains for each spectrum. This was done by the MCMC package integrated in XSPEC. The parameters and the associated errors are given in Table 4. The significance of the line was then calculated as the fraction of the iterations where the line normalization parameter was non-zero. We see in Table 4 that the 6.4 keV line in the *XMM* observation and 6.7 keV lines in the *Suzaku* and *Chandra* observations are significant at a level of over 99.99%. The significance for the 6.9 keV line in the *XMM* observation is about 97%, and only less than 90% for the 6.4 keV lines in the *Suzaku* and *Chandra* observations. As in Figure 6, we plot the probability contours of line energy and line normalization derived from the MCMC analysis in the upper panel of Figure 7 at probability levels of 4×10^{-4}, 8×10^{-4}, and 1.2×10^{-3}. Histograms showing the distribution of each line normalization are also shown in the lower panel of Figure 7. The left plot shows the neutral 6.4 keV line normalization distribution and the right plot shows the ionized line (6.7 or 6.9 keV) distributions. Lines in black, blue, and red indicate the observation of *XMM*, *Suzaku*, and *Chandra*, respectively. The peak of distribution of the 6.4 keV line overlaps in the *Suzaku* and *Chandra* observations, but is obviously separated from the *XMM* observation, giving a ∼90% probability of the line variability. However, the variability of the ionized iron line is not significant as indicated by the right panel of Figure 7.

We also tried to use three lines to fit the iron emission spectra; however, the data quality does not allow us to investigate the possibility that both He-like and H-like lines are present.

3.6. Off-nuclear Point Source

Ultraluminous X-ray objects (ULXs) are commonly seen in ULIRGs (Ptak et al. 2003). They are objects that are much more luminous than a stellar mass black hole or neutron star binary accreting at Eddington limit, and are not located in the nucleus of a galaxy. As shown in Figure 1, an off-nuclear point source (X1) is found about 8″ south of the southern nucleus, which is also detected by wavdetect. No counterpart at this position is found in optical images. We plot the light curve of X1 in Figure 8 within the three *Chandra* exposures, and the bin size is 2 ks. The
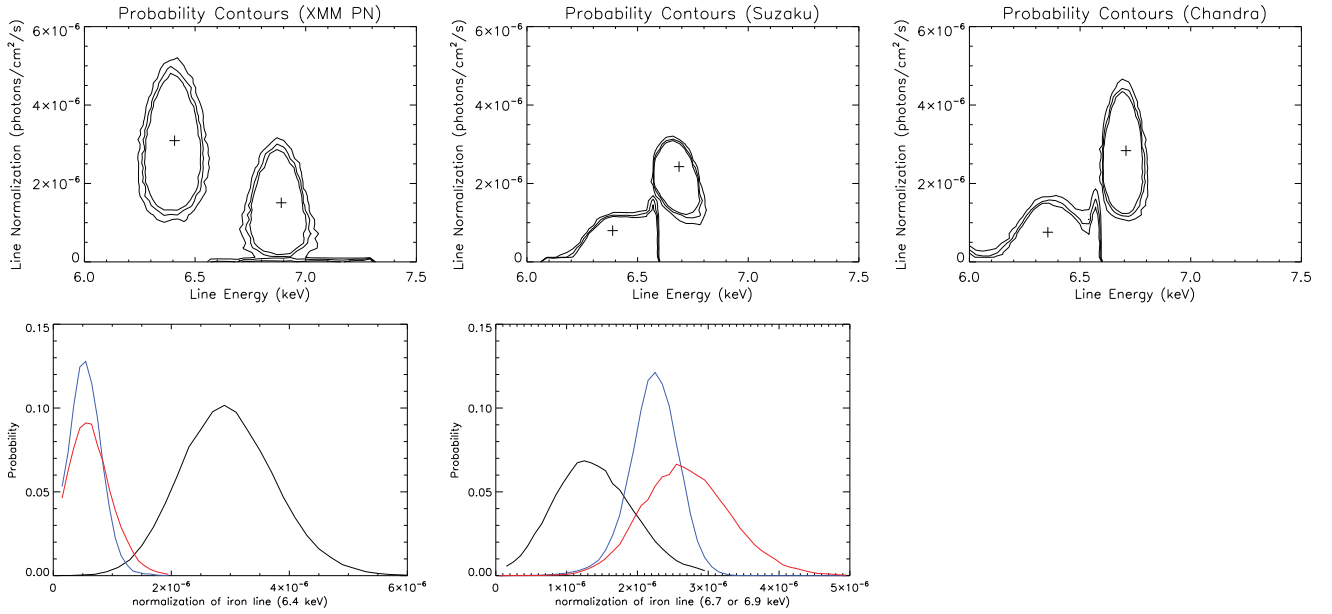
Figure 7. Upper: probability contours of the iron lines from MCMC. The contour levels correspond to probabilities of 4×10^{-4}, 8×10^{-4}, and 1.2×10^{-3}. Lower: distribution of the normalization parameter of the iron line component at 6.4 keV (left) and 6.7 or 6.9 keV (right) in *XMM* (black), *Suzaku* (blue), and *Chandra* (red) observations. The parameter probability is in arbitrary units, and the relative scale depends on the bin size.
(A color version of this figure is available in the online journal.)

Table 4
Iron Emission Line Features

Observation	Spectral Fit						
	Line 1				Line 2		
	E	σ	EW		E	σ	EW
XMM	$6.40^{+0.12}_{-0.13}$	$0.13^{+0.27}_{-0.09}$	$1.16^{+0.94}_{-0.50}$		$6.89^{+0.07}_{-0.08}$	0.01 (fix)	$0.44^{+0.32}_{-0.33}$
Suzaku	$6.39^{+0.30}_{-0.30}$	0.01 (fix)	$0.09^{+0.06}_{-0.06}$		$6.69^{+0.04}_{-0.04}$	$0.10^{+0.06}_{-0.05}$	$0.48^{+0.12}_{-0.11}$
Chandra	$6.43^{+0.37}_{-0.36}$	0.1 (fix)	$0.17^{+0.17}_{-0.17}$		$6.71^{+0.07}_{-0.03}$	$0.04^{+0.09}_{-0.04}$	$0.66^{+0.41}_{-0.26}$

Observation	MCMC							
	Line 1				Line 2			
	E	σ	EW	Significance	E	σ	EW	Significance
XMM	$6.41^{+0.10}_{-0.09}$	$0.13^{+0.07}_{-0.08}$	$1.15^{+0.54}_{-0.48}$	>99.99%	$6.89^{+0.10}_{-0.09}$	0.01 (fix)	$0.44^{+0.32}_{-0.34}$	97.14%
Suzaku	$6.41^{+0.18}_{-0.13}$	0.01 (fix)	$0.09^{+0.08}_{-0.09}$	87.79%	$6.69^{+0.06}_{-0.06}$	$0.11^{+0.09}_{-0.03}$	$0.47^{+0.11}_{-0.13}$	>99.99%
Chandra	$6.35^{+0.21}_{-0.28}$	0.1 (fix)	$0.14^{+0.17}_{-0.14}$	81.16%	$6.71^{+0.06}_{-0.05}$	$0.08^{+0.02}_{-0.03}$	$0.89^{+0.37}_{-0.31}$	>99.99%

Note. E, σ, and EW are in units of keV.

spectra of the non-nuclear point source were extracted from a circle of $2''$ radius, and the background region was chosen to be a concentric annulus with an inner radius of $4''$ and an outer radius of $5''$. This point source has 78 photon counts in the 0.3–8 keV band detected in three exposures. Thus, we binned the summed spectrum into at least 1 count per bin using Cash statistics to perform the spectral fit.

We fitted the spectrum of this point source with several models: simple PL, a thermal plasma (APEC) plus a PL, and a multi-color accretion disk (MCD) with a PL. Table 5 lists the best-fitting parameters and the observed soft and hard X-ray luminosities of each model. The best-fitting photon index is $2.03^{+0.81}_{-0.65}$ in the PL model and $2.07^{+0.77}_{-0.71}$ in the APEC+PL model, and a little bit harder ($1.58^{+0.38}_{-0.30}$) in the MCD+PL model. The temperature of the plasma in the APEC model is found to be $kT = 0.29^{+0.18}_{-0.11}$ keV, and the temperature at inner disk radius of the MCD model is $kT_{\rm in} = 0.46^{+0.07}_{-0.14}$ keV. All three models give

the observed soft X-ray luminosity of about 2.4×10^{40} erg s^{-1}, and the hard X-ray luminosity of about 4×10^{40} erg s^{-1}, which is about one order of magnitude more luminous than a typical ULX.

4. DISCUSSION

The *Chandra* observation allows us to disentangle the two nuclei in the merger system of IRAS 19245−7245 for the first time in X-ray imaging. Our analysis demonstrates that the southern nucleus, which hosts a Compton-thick AGN, contributes over 80% of the X-ray emission of the entire merger system in 0.5–10 keV band, and produces ∼90% of the hard X-ray luminosity. Extended soft X-ray emission has been observed around the southern nucleus out to a radius of ∼25 kpc, contributing a similar amount of soft X-ray photons as the southern nucleus itself.
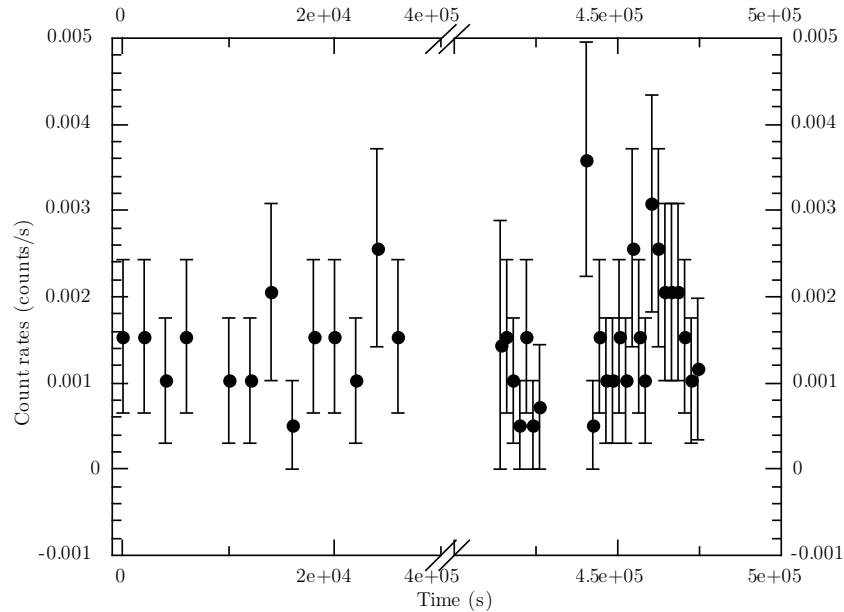
Figure 8. Light curve of X1 with bin size of 2 ks obtained from the three *Chandra* exposures. The time axis is broken for display purpose, and the origin of this axis corresponds to the starting time of ObsID 10538.

Table 5
Spectral Fits Parameters of the Off-nuclear Point Source (X1)

Model	N_H ($\times 10^{21}$ cm^{-2})	kT or kT_{in} (keV)	Γ	C-statistic /dof	$L_{0.5-2\,keV}$ ($\times 10^{40}$ erg s^{-1})	$L_{2-10\,keV}$ ($\times 10^{40}$ erg s^{-1})
PL	$1.37^{+0.81}_{-0.67}$		$2.03^{+0.82}_{-0.65}$	50.0/55	$2.4^{+0.5}_{-0.4}$	$4.1^{+0.9}_{-0.8}$
APEC+PL	$2.79^{+0.79}_{-0.76}$	$0.29^{+0.18}_{-0.11}$	$2.07^{+0.77}_{-0.71}$	49.0/53	$2.3^{+0.6}_{-0.5}$	$4.0^{+1.1}_{-0.9}$
MCD+PL	$N_{H,G}$	$0.46^{+0.07}_{-0.14}$	$1.58^{+0.38}_{-0.30}$	49.7/54	$2.4^{+2.1}_{-1.8}$	$4.5^{+1.4}_{-1.2}$

4.1. Emission from AGNs

Soft emission. The flat hard X-ray continuum and the intrinsic Compton-thick absorber have been well discussed by Braito et al. (2003, 2009). One of the key goals of our *Chandra* observation was to better investigate the relative contribution of SB and AGN activity. However, this discrimination becomes vague when referring to the soft emission from the southern nucleus. The soft emission is fit well with a PL and a thermal component. The properties of the thermal component are consistent with those from the extended region and thus are likely to be thermal- and SB-dominated emission rather than AGN-photoionized plasma. Even when we extracted the emission from a smaller region, this thermal component could not be ruled out. The total observed 0.5–2 keV luminosity of the southern nucleus is $\sim 2.6 \times 10^{41}$ erg s^{-1}, and one-third comes from the thermal emission according to the spectral model. If we convert the soft X-ray luminosity to SFR assuming the relationship given by Ranalli et al. (2003), we get SFR $\sim 57\,M_\odot$ yr^{-1}, which is close to the estimated SFR that is about $80\,M_\odot$ yr^{-1} for the southern nucleus (Berta et al. 2003) given the dispersion in the X-ray/SFR correlation.

Fe Kα line. Iron emission lines are only detected in the southern nucleus. We tried to add a Gaussian component in the spectral fitting of the inner region D1 in the extended SB region, however, it did not reduce the χ^2. The low quality of the hard X-ray photons in the outer region D2 prevents us from investigating the iron line feature. Indeed, the 6–7 keV image shows that iron line photons are only from the southern nucleus. The luminosity of the iron emission line observed by *XMM-Newton* in 2001 March is 3.3×10^{41} erg s^{-1} (after *K*-correction), and it dropped to 2.2×10^{41} erg s^{-1} in the *Suzaku* observation in 2005 November. The iron line luminosity from our recent *Chandra* observation is, however, consistent with the *XMM* observation. The EW of line was 1.5 keV and 0.7 keV in *XMM* and *Suzaku* observations, respectively.

We also investigated the possibility of a blend of two lines of the Fe Kα emission. In the 2001 *XMM* observation, a neutral iron line with centroid line energy at 6.4 keV and an ionized H-like iron line with centroid line energy at 6.9 keV are clearly separated at significance level >99%. The intensity of the 6.4 keV line is larger than the 6.9 keV line. However, the significance of the 6.4 keV line in the 2005 *Suzaku* and 2009 *Chandra* observations decreases to only 2σ, and an He-like iron line (6.7 keV) shows up in the late two observations and dominates the intensity. Terashima et al. (2000) reported a similar iron line variability in NGC 4579 in two *ASCA* observations, but Eracleous et al. (2002) compared that with a *Chandra* observation and argued that such variability might be due to the very large extraction region of *ASCA* spectra, which was contributed by the ionized Fe Kα emission from the entire circumnuclear nebula. However, as we show in above sections that there is little extended emission in 6–7 keV band, the aperture effect is not likely the cause of the variability.

The variability of the 6.4 keV line indicates that the cold matter where this line originates within a compact region from the nucleus. If the energy shift of the ionized line from 6.9 keV to 6.7 keV is true, there might be multiple locations of the clumpy clouds with different ionization states. Since there is no flux
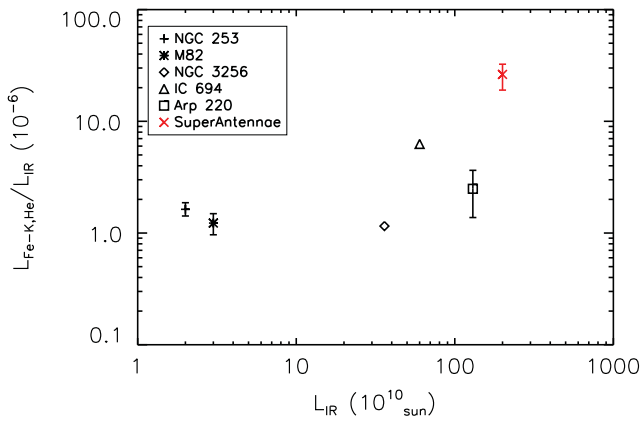
Figure 9. Ratio of helium-like Fe–K line luminosity to the infrared luminosity of the local (U)LIRGs and starburst galaxies and comparison with the Superantennae. Their values are taken from literature, and no error bars for NGC 3256 and IC 694 are reported in their references.

(A color version of this figure is available in the online journal.)

Table 6
Physical Properties of the Diffuse Hot Gas in Regions S, D1, and D2

Parameters	S	D1	D2
n_e (10^{-2} cm^{-3})	$5.5f_0^{-1/2}$	$0.44f_1^{-1/2}$	$0.087f_2^{-1/2}$
M ($10^8\,M_\odot$)	$2.5f_0^{1/2}$	$7.2f_1^{1/2}$	$10.3f_2^{1/2}$
$\dot{M}$ ($M_\odot$ yr^{-1})	$39f_0^{1/2}$	$47f_1^{1/2}$	$48f_2^{1/2}$
E (10^{56} erg)	$8.7f_0^{1/2}$	$25f_1^{1/2}$	$36f_2^{1/2}$
$\dot{E}$ (10^{42} erg s^{-1})	$4.3f_0^{1/2}$	$5.2f_1^{1/2}$	$5.3f_2^{1/2}$
P (10^{-10} dyn cm^{-2})	$1.6f_0^{-1/2}$	$0.13f_1^{-1/2}$	$0.025f_2^{-1/2}$

Notes. f_0, f_1, and f_2 are the volume filling factors of the X-ray-emitting material in regions of S, D1, and D2, respectively. See the text for details.

variability of the continuum emission, we could not constrain the distance of the ionized line emitters based on the time lag between the continuum and the Fe line ionization change. If the change of ionization state (from H-like to He-like) is not real but is instead the result of the insufficient photons in the spectral fitting, there is still a ∼70% change in the ionized Fe Kα line intensity. The 6.7 keV line could originate either from an ionized accretion disk or from reflection/scattering of the hard nuclear X-rays by ionized clouds. Assuming the observed variability of 6.7 keV line is real, what is the size of ionized line emitter? From the timescale of the three observations, we can simply estimate the upper limit of a few pc. However, this value is too large if the line emission is reflected by the Compton-thick cloud. Assuming the ionization parameter $\xi \sim 3000$ erg cm s^{-1} is constant throughout the cloud, the inner radius of the cloud is $r_{in} = L_{in}/\xi N_H \sim 0.01$ pc, where $L_{in} \sim 3 \times 10^{44}$ erg s^{-1} is the intrinsic AGN luminosity estimated by Braito et al. (2009), and the density at 0.01 pc is ∼10^8 cm^{-3}. If the ionized reflection matter is warm Compton-thin gas filling the space between the neutral Compton-thick reprocessor (see the discussion in Braito et al. 2009), the location of the gas can extend to ∼0.1–1 pc.

Rather than photoionization by AGN, another possible origin of the ionized Fe–K line could be the hot gas produced by the SB. In order to test this possibility, we show in Figure 9 the ratio of the helium-like Fe–K line luminosity to the IR luminosity ($L_{Fe-K,He}/L_{IR}$) of the Superantennae and compare its value to those of nearby (U)LIRGs and SBs, e.g., NGC 253 (Mitsuishi et al. 2011), M82 (Strickland & Heckman 2007), NGC 3256 and IC 694 (Pereira-Santaella et al. 2011), and Arp 220 (Iwasawa et al. 2005). The values of iron line luminosity and its uncertainty of each galaxy are taken from the corresponding references, in which the $L_{Fe-K,He}$ uncertainty of NGC 3256 and IC 694 were not reported. The ratio for the Superantennae is about one order of magnitude higher than the other SB galaxies that show extended helium-like Fe–K emission. Therefore, the higher excess of $L_{Fe-K,He}/L_{IR}$ indicates that the iron line emission in the Superantennae is not dominated by the SB process.

4.2. Emission from Starburst

Soft emission. From the soft X-ray image of IRAS 19245−7245, we can see that hot gas emission extends to a radius of ∼20″ (∼25 kpc) surrounding the southern nucleus. The thermal emission requires a $kT \sim 0.8$ keV component in

the best-fitting models of the inner region (D1) of the diffuse emission. The temperature is consistent with the thermal emission found in the southern nucleus. Although the spectra in the outer region (D2) have relatively poorer quality, the temperature of the hot gas in D2 from the spectral fit is consistent with that of D1 but with larger uncertainty.

Using the parameters of the X-ray spectral model, we can derive the basic physical properties of the hot gas in the regions of S, D1, and D2. The normalization for the APEC component ($10^{-14} \int n_e n_H dV/4\pi [D_A(1+z)]^2$) implies a volume integral of density squared if we assume the electron density (n_e) approximately equals the H atom density (n_H), where $D_A = 243.3$ Mpc is the angular distance of IRAS 19254−7245 at redshift $z = 0.062$. The mass ($M = n_e m_H V$, where m_H is the mass of hydrogen atom and V is the gas volume), mean thermal pressure ($P = 2n_e kT$), and total thermal energy ($E = PV$) of the hot gas can be derived using the electron density and temperature from the spectral fit. The characteristic timescale could be calculated as the size divided by the sound speed in the hot gas. Then, the outflow rates of the mass ($\dot{M}$) and energy ($\dot{E}$) can be roughly estimated according to the timescale. These physical parameters are listed in Table 6, where we parameterize them by the volume filling factor f of the X-ray-emitting material. We see that while most of the mass and thermal energy content of the hot gas is contained in the outer regions (D1 and D2), the actual estimates of the rates at which energy and mass flow outward are consistent as we move from the central region (S) to D1 and through D2. This is consistent with a mass- and energy-conserving outflow that originates in the SB (inside region S).

We then use Starburst99 (Leitherer et al. 1999) to estimate the relevant parameters expected for the collection of supernovae and massive stars in the SB. We adopt an SFR of 80 $M_\odot$ yr^{-1} (Berta et al. 2003) that has been constant over the past 100 Myr and has a standard Kroupa IMF. The resulting total mechanical power of the stellar wind and supernovae ejecta is 4×10^{43} erg s^{-1}, they carry a momentum flux of 3×10^{35} dyn, and the mass outflow rate is $\dot{M}_{SN} \sim 16\ M_\odot$ yr^{-1}.

These values imply that an SB-driven outflow can account for the properties of the extended soft X-ray emission. The observed outflow rate of (thermal) energy is only 10% of the total energy injection rate from the SB while the observed mass outflow rate is about three times larger than the expected SB mass injection rate. This latter result is commonly observed in SB-driven winds and it ascribed to mass loading as the supernovae and massive star ejecta mix with ambient interstellar gas (e.g., Strickland & Heckman 2009). The predicted momentum flux from the SB results in a wind ram pressure of about 1.8×10^{-10}, 1.6×10^{-11}, and 4×10^{-12} dyn cm^{-2} at the outer boundaries of regions S,
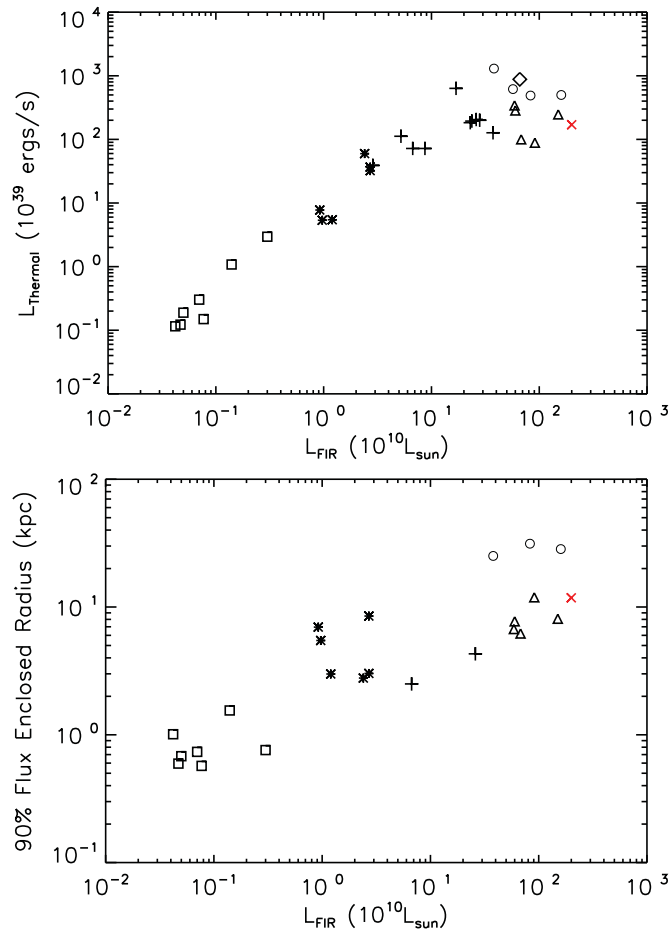
Figure 10. Total thermal X-ray luminosity (upper) and the radius enclosing 90% of the total flux in the 0.3–2.0 keV X-ray band (lower) vs. the far-IR luminosity. IRAS 19254−7245 is marked in red cross symbol. Other sources in this plot are dwarf starbursts (square), starbursts (asterisk), NGC 6240 (diamond), Lyman break analogs (plus), starburst-dominated ULIRGs (triangle), and AGN ULIRGs (circle), which are taken from Grimes et al. (2005, 2006, 2007) and Jia et al. (2011).

(A color version of this figure is available in the online journal.)

D1, and D2, respectively. These values are very close to the inferred pressures in the observed extended soft X-ray region.

More empirically, we can compare the basic properties of the soft extended emission to what is seen in typical SBs. First, we can compare the relation between the far-IR and soft X-ray luminosities of IRAS 19245−7245 with other star-forming galaxies that differ in their size and luminosity. The plot is shown in the upper panel of Figure 10, where the other galaxies are dwarf SBs, normal SBs, Lyman break analogs, SB-dominated ULIRGs, and AGN ULIRGs (Grimes et al. 2005, 2006, 2007; Jia et al. 2011). The soft X-ray luminosities are derived from the thermal component in the spectral fits by excluding the contribution from AGNs and X-ray binaries. The luminosity ratio of SX/IR for ULIRGs is found to be about 1 dex smaller than the value for star-forming galaxies with $L_{IR} < 10^{11} \, L_{\odot}$. This deficiency in systems with high IR luminosity was characterized as $\langle \log L_{SX}/L_{IR} \rangle = -4.55$ with 1σ scatter of 0.37 by Symeonidis et al. (2011). This ratio for IRAS 19245−7245 is −4.66 according to our spectral analysis, well consistent with their result for the star-forming galaxies with similarly high far-IR luminosities. We also show in the lower panel of Figure 10 that IRAS 19245−7245 obeys the

relation between the size of the soft X-ray-emitting region and the far-IR luminosity defined by other star-forming galaxies.

We conclude that the properties of the large (∼50 kpc diameter) spatially extended region of soft X-ray emission are entirely consistent with an origin as an SB-powered galactic wind.

Hard emission. The hard X-ray continuum of the diffuse emission is characterized as a PL with photon index of $\Gamma \sim 1.8$, which is much steeper than that found in the southern nucleus. We compare the luminosity ratio of hard X-ray to far-IR with other LIRGs and ULIRGs observed by *Chandra* in Figure 11. The other samples are from Iwasawa et al. (2009) and Lehmer et al. (2010), where Iwasawa et al.'s sample was divided into groups of AGNs and "hard X-ray quiet" galaxies (HXQs) indicated by diamond and asterisk symbols, respectively, and Lehmer et al.'s sample is indicated by triangle symbols. We show IRAS 19254−7245 as plus signs in two positions in this plot: one with AGN contribution included (in red) and the other one without AGN contribution (in blue). We see that the hard X-ray luminosity after subtracting the AGN contribution is consistent with other pure star-forming galaxies (with no AGN) having similar far-IR luminosities.

4.3. Emission from Other Regions

Northern nucleus. The northern nucleus was not resolved in the *XMM-Newton* observation, and it was included in the 15″ extraction circle of spectral analysis (Braito et al. 2003). According to our *Chandra* observation, both the soft and hard X-ray luminosities are ∼30 times smaller than those of the southern nucleus. We fitted the spectrum of northern nucleus with only an absorbed PL due to the limited photons we obtained. The photon index is found to be $\Gamma = 1.25$ but poorly constrained. It has been demonstrated by the optical spectra that there is no AGN emission in this nucleus. This classification is supported by its low X-ray luminosity and the non-detection of Fe Kα line emission in our *Chandra* observation. The SFR of the northern nucleus is only ∼0.5 $M_{\odot}$ yr^{-1}, and it appears to be in a post-SB phase (Berta et al. 2003), which is consistent with its weak X-ray emission.

Off-nuclear point source. One off-nuclear point source is found ∼8″ south of the southern nucleus. If we assume that it is associated with the Superantennae, it would lie about 9.4 kpc from the southern nucleus in projection and have a 0.5–10 keV luminosity as high as 6×10^{40} erg s^{-1} (based on the spectral fits using different models). This is about one order of magnitude more luminous than the typical ULXs found in other galaxies, but still within the luminosity range they span. In a recent *Chandra* survey of X-ray point sources in nearby galaxies, Liu (2011) found 479 ULXs with $L_X(0.3–8 \, keV) \geqslant 2 \times 10^{39}$ erg s^{-1}, and about 15% (74 out of 479) are extreme ULXs with $L_X(0.3–8 \, keV) \geqslant 10^{40}$ erg s^{-1}. The X-ray luminosity of this ULX in the Superantennae would imply a minimum black hole mass of about 500 $M_{\odot}$ for a source at the Eddington limit. We note that an association with the Supernantennae is likely. Using the 2–8 keV flux of ∼4×10^{-15} erg cm^{-2} s^{-1} and the number–count relations from Chandra Deep Fields (Bauer et al. 2004; Brandt & Hasinger 2005), we calculate that the possibility of a background AGN located within a radius of 8″ from the southern nucleus is only about ∼1.5%.

5. SUMMARY

In this work, we have presented *Chandra* observation of the prototypical merger/ULIRG IRAS 19254−7245 (the
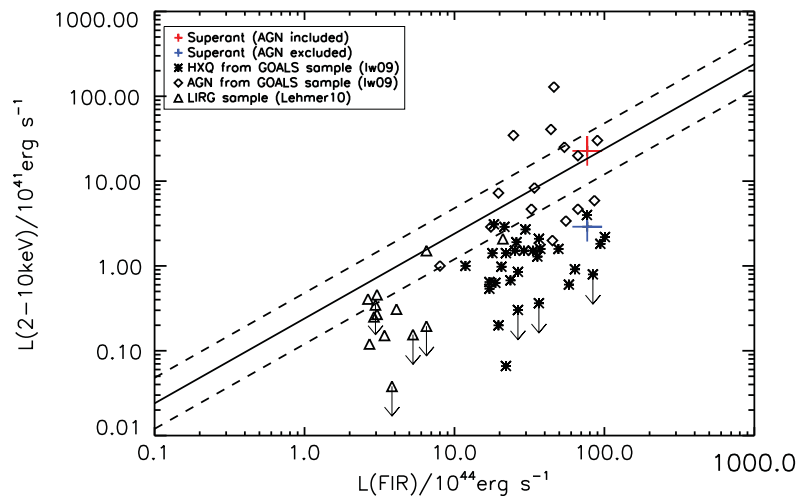
Figure 11. Hard X-ray luminosity vs. far infrared luminosity. IRAS 19254−7245 is marked by plus sign in red (entire galaxies including the AGN) and in blue (without the AGN). Others are from Iwasawa et al. (2009, hereafter Iw09) and Lehmer et al. (2010, hereafter Lehmer10) for comparison, where the diamond symbols indicate the Iw09 AGN samples, and asterisks and upper limit arrows are "hard X-ray quiet" galaxies (HXQs) from Iw09, and LIRG samples from Lehmer10 are marked as triangles.

(A color version of this figure is available in the online journal.)

Superantennae). This is the first X-ray observation that could spatially resolve the diffuse emission of this ULIRG. The main results are summarized as follows:

1. The southern nucleus hosts a Compton-thick AGN, which contributes ∼90% of the hard X-ray emission of IRAS 19254−7245. The soft X-ray emission from the AGN region is contaminated by the circumnuclear SB.

2. The diffuse emission from SB extends out to a radius of about 25 kpc surrounding the southern nucleus, and is dominated by thermal emission with a temperature of ∼0.8 keV. This emission accounts for ∼33% of the soft emission from the whole merging system.

3. The global properties of the extended thermal emission are consistent with winds seen in many SBs and the basic physical properties are fully consistent with an outflow driven by the supernovae and massive stars in the SB.

4. The prominent Fe Kα emission line is a blend of both neutral and ionized lines. The neutral line shows flux variability, indicating that the iron line emission comes from a compact region in the southern nucleus.

5. No evidence for an AGN in the northern nucleus is detected in this *Chandra* observation. An off-nuclear point source is found and could be classified as a ULX if it is associated with the Superantennae.

REFERENCES

Bauer, F. E., Alexander, D. M., Brandt, W. N., et al. 2004, AJ, 128, 2048
Berta, S., Fritz, J., Franceschini, A., Bressan, A., & Pernechele, C. 2003, A&A, 403, 119
Braito, V., Franceschini, A., Della Ceca, R., et al. 2003, A&A, 398, 107
Braito, V., Reeves, J. N., Della Ceca, R., et al. 2009, A&A, 504, 53
Brandt, W. N., & Hasinger, G. 2005, ARA&A, 43, 827
Carter, C., Karovska, M., Jerius, D., Glotfelty, K., & Beikman, S. 2003, in ASP Conf. Ser. 295, Astronomical Data Analysis Software and Systems XII, ed. H. E. Payne, R. I. Jedrzejewski, & R. N. Hook (San Francisco, CA: ASP), 477
Cash, W. 1979, ApJ, 228, 939
Chevalier, R. A., & Clegg, A. W. 1985, Nature, 317, 44

Dahlem, M., Weaver, K. A., & Heckman, T. M. 1998, ApJS, 118, 401
Della Ceca, R., Ballo, L., Tavecchio, F., et al. 2002, ApJ, 581, L9
Dickey, J. M., & Lockman, F. J. 1990, ARA&A, 28, 215
Eracleous, M., Shields, J. C., Chartas, G., & Moran, E. C. 2002, ApJ, 565, 108
Franceschini, A., Braito, V., Persic, M., et al. 2003, MNRAS, 343, 1181
Fruscione, A., McDowell, J. C., Allen, G. E., et al. 2006, Proc. SPIE, 6270, 62701V
Gallagher, S. C., Brandt, W. N., Chartas, G., Garmire, G. P., & Sambruna, R. M. 2002, ApJ, 569, 655
Genzel, R., Lutz, D., Sturm, E., et al. 1998, ApJ, 498, 579
Genzel, R., Tacconi, L. J., Rigopoulou, D., Lutz, D., & Tecza, M. 2001, ApJ, 563, 527
Grimes, J. P., Heckman, T., Hoopes, C., et al. 2006, ApJ, 648, 310
Grimes, J. P., Heckman, T., Strickland, D., et al. 2007, ApJ, 668, 891
Grimes, J. P., Heckman, T., Strickland, D., & Ptak, A. 2005, ApJ, 628, 187
Heckman, T. M., Armus, L., & Miley, G. K. 1990, ApJS, 74, 833
Heckman, T. M., Lehnert, M. D., & Armus, L. 1993, in The Environment and Evolution of Galaxies, ed. J. M. Shull & H. A. Thronson (in Astrophysics and Space Science Library, Vol. 188; Dordrecht: Kluwer), 455
Hopkins, P. F., Somerville, R. S., Hernquist, L., et al. 2006, ApJ, 652, 864
Iwasawa, K., & Comastri, A. 1998, MNRAS, 297, 1219
Iwasawa, K., Sanders, D. B., Evans, A. S., et al. 2005, MNRAS, 357, 565
Iwasawa, K., Sanders, D. B., Evans, A. S., et al. 2009, ApJ, 695, L103
Jia, J., Ptak, A., Heckman, T. M., et al. 2011, ApJ, 731, 55
Kalberla, P. M. W., Burton, W. B., Hartmann, D., et al. 2005, A&A, 440, 775
Lehmer, B. D., Alexander, D. M., Bauer, F. E., et al. 2010, ApJ, 724, 559
Leitherer, C., Schaerer, D., Goldader, J. D., et al. 1999, ApJS, 123, 3
Liu, J. 2011, ApJS, 192, 10
Magdziarz, P., & Zdziarski, A. A. 1995, MNRAS, 273, 837
Mirabel, I. F., Lutz, D., & Maza, J. 1991, A&A, 243, 367
Mitsuishi, I., Yamasaki, N. Y., & Takei, Y. 2011, ApJ, 742, L31
Nardini, E., Risaliti, G., Salvati, M., et al. 2008, MNRAS, 385, L130
Pappa, A., Georgantopoulos, I., & Stewart, G. C. 2000, MNRAS, 314, 589
Pereira-Santaella, M., Alonso-Herrero, A., Santos-Lleo, M., et al. 2011, A&A, 535, A93
Ptak, A., Heckman, T., Levenson, N. A., Weaver, K., & Strickland, D. 2003, ApJ, 592, 782
Ptak, A., Serlemitsos, P., Yaqoob, T., & Mushotzky, R. 1999, ApJS, 120, 179
Ranalli, P., Comastri, A., & Setti, G. 2003, A&A, 399, 39
Risaliti, G., Maiolino, R., Marconi, A., et al. 2003, ApJ, 595, L17
Sanders, D. B., & Mirabel, I. F. 1996, ARA&A, 34, 749
Springel, V., Di Matteo, T., & Hernquist, L. 2005, MNRAS, 361, 776
Strickland, D. K., & Heckman, T. M. 2007, ApJ, 658, 258
Strickland, D. K., & Heckman, T. M. 2009, ApJ, 697, 2030
Strickland, D. K., & Stevens, I. R. 2000, MNRAS, 314, 511
Symeonidis, M., Georgakakis, A., Seymour, N., et al. 2011, MNRAS, 417, 2239
Teng, S. H., Wilson, A. S., Veilleux, S., et al. 2005, ApJ, 633, 664
Terashima, Y., Ho, L. C., Ptak, A. F., et al. 2000, ApJ, 535, L79
Veilleux, S., Kim, D.-C., Peng, C. Y., et al. 2006, ApJ, 643, 707
Veilleux, S., Kim, D.-C., & Sanders, D. B. 2002, ApJS, 143, 315